THE INTEGRATED OPTIC RF SPECTRUM ANALYZER

M.E. Pedinoff and T.R. Ranganath
Hughes Research Laboratories
3011 Malibu Canyon Road
Malibu, California 90265
(213) 456-6411

T.R. Joseph
Hughes Ground Systems Group
Fullerton, CA 92634

J.Y. Lee
Hughes Industrial Products Division
Carlsbad, CA 92008

ABSTRACT

The performance of a fully integrated rf optical spectrum analyzer (IOSA) is presented. This device exhibited a 3 dB bandwidth of 380 MHz with a diffraction efficiency of 5% (at 500 MW rf power). The fully integrated device operating at $\lambda_o = 0.82\mu$ exhibited the following performance figures: an acousto-optic bandwidth of 380 MHz, a 3 dB spot size of $\sim$8 MHz, a two-tone resolution of 8 MHz, and a linear dynamic range of >25 dB as observed visually on an oscilloscope. The resolution uniformity across the rf bandwidth is presently limited by the mechanical position errors of the semiconductor laser and the detector/CCD array in the focal planes of the collimating and focusing geodesic lenses.

All components used in the IOSA were first tested individually and reported here. A fully functional (with no dead detector cells) detector/CCD array exhibited a linear dynamic range of 30 dB, with a sensitivity uniformity of $\pm$1 dB. A measurement of the undeflected zeroth order beam indicates geodesic lens insertion losses of $\lesssim$2 dB each. The acoustic transducer exhibited a 400 MHz 3 dB rf bandwidth.

INTRODUCTION

The use of guided-wave optics resulted in the development of a new class of one-dimensional optical processors that have a rigid, compact optical design and a low electrical drive power requirement. This type of processor is most easily applied to the analysis of rf signal spectra. In this paper we describe an integrated-optics circuit for real-time rf spectral analysis (ref. 1,2).

An integrated-optics optical spectrum analyzer consists of an injection laser diode, a thin-film optical waveguide, waveguide lenses, a surface acoustic wave (SAW) transducer, and a linear detector array. This device employs the interaction between a coherent optical wave and an acoustic wave driven by an input electrical signal to determine the power spectral density of the input. The basic design layout of an integrated-optic spectrum analyzer (IOSA) is shown in Figure 1. An incoming radar signal is mixed with a local oscillator so that the intermediate frequency (IF) is

within the passband of the transducer. After amplification, the signal is applied to the SAW transducer. The resultant SAWs traversing the optical waveguide generate a periodic modulation of the refractive index of the waveguide mode. If a collimated, guided optical beam intersects the acoustic beam at the Bragg angle, a portion of the beam will be diffracted (deflected) at an angle closely proportional to the acoustic frequency, and with an intensity proportional to the power level of the input signal. The Bragg deflected light is then focused onto an array of focal plane detectors where each detector output becomes one frequency channel of the spectrum analyzer.

ACOUSTO-OPTIC INTERACTION

A diagram of the acousto-optic interaction region in a monolithic integrated optic structure is shown in Figure 2. The criterion for an efficient Bragg diffraction is that the interaction length L be sufficiently large so that the parameter Q is larger than 1; i.e.,

$$Q = \frac{L\lambda o}{n\Lambda^2 \cos \theta_i} > 1 \quad ,$$

where n is the waveguide modal index, Λ is the acoustic wavelength, λo is the optical wavelength, and θ_i is the incident angle of the optical beam defined in Figure 2. This criterion physically corresponds to an interaction length larger than the acoustic wavelength. The diffracted energy appears predominantly in one order.

When the acousto-optic interaction is phase matched in first order Bragg diffraction, the angle of incidence, θ_i, and the angle of diffraction, θ_d, are equal. The angular deflection δ (the angle between the incident and diffracted beam, or twice the Bragg angle) is given by

$$\delta = \theta_i + \theta_d = 2 \sin^{-1} \left(\frac{\lambda_o}{2n\Lambda} \right)$$

This angle is different for each acoustic wavelength or frequency. For a fixed incident optical beam direction, the direction of the acoustic wave must change with frequency. Within the small angle approximation, the deflection angle is linearly related to the acoustic frequency by

$$\frac{d\delta}{df_s} = \frac{\lambda_o}{nv_s} \quad ,$$

where f_s is the acoustic frequency, and v_s is the velocity of the surface acoustic wave. When the acousto-optic medium exhibits significant dispersion in v_s the deflection equation takes the form

$$\frac{d\delta}{df_s} = \frac{\lambda_o}{nv_s}\left(1 - \frac{f_s}{v_s}\frac{dv_s}{df_s}\right)$$

This indicates that nonlinear spacing of detector elements in the focal plane must be used for dispersive acoustic materials.

A complete Fourier transform analysis for this device was reported earlier (ref. 2). In this device the deflected optical beam generated in the Bragg cell modulator is proportional to the product of the incident optical beam wavefront, the accoustic wavefront, and the efficiency of the interaction. Therefore, as a result of the acousto-optic interaction, a fraction of the transmitted light beam acquires a new direction of propagation, corresponding to a bandwidth, df_s, centered at frequency f_s.

The output intensity distribution thus displays, at a position linearly proporional to the frequency of the modulating signal, a signal whose intensity is proportional to the intensity of the deflected beam (i.e., proportional to the spectral component of frequency f_s, multiplied by the efficiency of the Bragg modulator). For a modulator with a flat response over the frequency range of interest, the output is thus proportional to the intensity of the spectral component.

DESIGN PARAMETER STUDY

The optical circuit design of an IOSA device is constrained by the required rf frequency resolution and the optical resolution limit set by the allowed crosstalk between adjacent cells. The rf frequency resoltuion requirement sets the upper limit of the detector cell size S

$$S \leq \frac{F\lambda_o}{nv_s}\Delta f \quad ;$$

while the optical resolution limit requires a minimum cell size determined by

$$S \geq \frac{g\lambda_o F}{nD} \quad ,$$

where D is the optical beam width, F is the output lens focal length, n is the effective guide index, and λ_o is the free-space wavelength. The resolution factor g is determined by the definition of optical focal spot resolution. These equations have been used to design an IOSA structure having 4 MHz rf resolution (ref.2) for an IOSA fabricated on an $LiNbO_3$ substrate, where the acoustic phase velocity is v_s = 3500 m/sec. For this device with a Gaussian beam truncated at the $1/e^2$ intensity points, the minimum beam width was 2.18 mm.

When the minimum optical beam width, D, is selected in the design, then the spot size of the optical beam at the detector array will just equal the detector cell size S. The adjacent channel crosstalk is defined as the total optical power collected by the cell adjacent to a cell corresponding to a given rf frequency divided by the total optical power collected by that rf frequency cell. This adjacent channel crosstalk ratio is plotted in Figure 3. The adjacent cell crosstalk is plotted as a function of DS. Thus, for an optical beam width of 2.18 mm, and a cell size of 8.0 μm (equal to the full lobe spot size at the focal plane), the crosstalk is -22.4 dB. If the lens quality is such that a lens diameter larger than D_{min} can be accommodated while diffraction-limited performance is still maintained, then the sidelobe intensity impinging on adjacent cells will be reduced. This will allow two closely spaced signals of significantly different energy levels to be detected and resolved. For a 4 MHz resolution and a cell size fixed by the full main lobe width of the minimum diameter beam (D_{min} = 2.18 mm), a 5.6 dB reduction in adjacent channel crosstalk results when the optical beam width is enlarged to three times this minimum value, or D = 6.54 mm. For this case, the adjacent channel crosstalk is -28 dB.

We have established that the value of $Sn/\lambda_o F$ necessary to achieve 4 MHz rf resolution is

$$\frac{Sn}{\lambda_o F} = 11.4 \times 10^{+2}\ m^{-1} \quad ,$$

where the ratio S/F for an $LiNbO_3$ system ($n \simeq 2.2$) operating at λ_o = 0.82 μm is $S/F = 4.25 \times 10^{-4}$. Since the detector cell size, S, is set by detector array design considerations, the focal length of the Fourier transform lens is required to be $F = (S/4.25) \times 10^4$, which, for an 8-μm cell size, is 18.8 mm. If the optical beam diameter is chosen to be 7.4 mm, then the f/no. of the output transform lens is f/2.54. For this system, the adjacent cell crosstalk due to the optical beam diffraction pattern is below -28 dB.

PROPAGATION MEDIUM

An important issue in the development of an IOSA was the selection of the optimum substrate material system from the available candidates. The material selected for this device was a y-cut $LiNbO_3$ substrate with propagation direction along either the z axis or 21.8° from the z axis. $LiNbO_3$ is considered to be one of the best acousto-optic materials because of its low acoustic propagation loss, high electromechanical coupling constant, and the relative absence of velocity dispersion due to the optical guiding layer. With this substrate material the detectors are interfaced by direct butt coupling to the $LiNbO_3$ waveguide. For y-cut crystals, $LiNbO_3$ substrates have different SAW characteristics for propagation along the z axis, and for propagation 21.8° off the z axis (ref. 3). An analysis of acousto-optic modulation efficiency indicated that there is no significant difference between these orientations. From the optical standpoint, the z-oriented acoustical transducers minimize the substrate anisotropy and are preferred.

The waveguide on the polished y-cut $LiNbO_3$ substrate is formed by in-diffusion of electron-beam-evaporated Ti (ref. 4). A fabrication sequence is used in which the important parameters (such as surface quality, optical flatness, cleanliness, uniformity, and adherence of the metal films to the substrate) are controlled throughout the process. Single-mode optical waveguides are formed by diffusing 200-Å-thick Ti at 950°C for 4 hours. The diffusion depth of the resulting waveguide is about 2 μm.

The propagation loss in $Ti:LiNbO_3$ waveguides at the He-Ne laser wavelength (λ = 6328 Å) is typically less than 1 dB/cm. The waveguide loss for a TE polarization wave (He-Ne laser wavelength) was experimentally determined to be 0.85 dB/cm (ref. 2).

In-plane scattering of the optical waveguide is an important parameter in determining the dynamic range of the IOSA. He-Ne laser light was used to excite the waveguide mode and the strength of the in-plane scattering was measured by scanning the m-line extracted by a coupling prism. The scattering intensity shown in Figure 4 is -40 dB for a scattering angle of 0.6° in the waveguide, corresponding to an acousto-optic deflection angle due to an acoustic frequency of 115 MHz. In-plane scattering levels of -49 dB and 57 dB of the peak intensity were measured at an in-plane scattering angle of 1.3° (corresponding to deflection by a SAW having a frequency of 270 MHz) on each side of the main beam. When the IOSA is operated at the GaAlAs laser wavelength, the in-plane scattering level is further reduced.

LASER CHARACTERIZATION

To meet the frequency resolution specification, the total output spectral width of the laser should be much less than 40 Å under operating conditions. Ideally, the output should be in a single transverse and single longitudinal mode with spectral width <1 Å. The lasing aperture should be as small as possible to simulate a point source so that the problem of collimating the laser output in the thin-film waveguide can be simplified. Based on these considerations, we selected the Hitachi GaAlAs buried-heterostructure injection laser diode as our source. The lasing aperture of the device is ∿1 μm in diameter with nearly isotropic divergence. In this program we tested two special-order lasers that have an emitting edge flush with the heat sink edge. They are double-heterojunction lasers, Model HLP2400, Serial Nos. 3831 and 3834. The far-field intensity distribution in the two principal orthogonal directions (perpendicular and parallel to the junction) was measured using a photomultiplier and a slit with an effective angular resolution of 0.115°. Figures 5 and 6 show the far-field intensity profile measured at HRL. The beam divergence in the plane parallel to the junction is less than 20° for both lasers. In the plane normal to the junction, the beam divergence is 30° (Serial No. 3834) and 37° (Serial No. 3831), respectively.

There is an upper limit in the laser power coupled into the waveguide at which the detector cell is saturated. The laser power requirement can be estimated based on the following values: a saturation charge density of the detector cells of 6.0×10^6 electrons/cell, a detector quantum efficiency of 0.25, a maximum acousto-optic deflection efficiency of 0.05, an optical propagation loss of 9 dB, and a detector integration time of 3.0 μsec. The calculation shows that about 600 μW of laser power has to be coupled into the waveguide.

WAVEGUIDE GEODESIC LENSES

Waveguide geodesic lenses are waveguide-covered depressions (or protrusions). The curvature of the depression generates a difference in geometric path length for rays traversing different portions of the structure; this produces a focusing effect. The optical path length at the center of the depression is longer than at the sides; and the phase fronts are curved toward the lens axis beyond the depression. If the depression is of a particular aspheric shape, or if the wavefront emerging from the line is appropriately compensated by external overlayers, the focusing will be aberration-free (except for field curvature).

The design of the aspherical depression profile for a diffraction-limited geodesic lens is based on the equivalent-lens principle (ref. 5). From a generalized Luneburg lens profile calculated by numerical computation, one can derive the equivalent aspherical geodesic lens profile. The geodesic lens has no chromatic aberrations because of its uniform refractive index. This is independent of dispersion in the material refractive index. The focal length of the geodesic lens is independent of the modal index, and it can be used in both single- and multi-mode optical systems.

Diffraction-limited geodesic lenses have been demonstrated in two different waveguide structures: polyurethane film-glass substrate (ref. 6) and Ti in-diffused $LiNbO_3$ waveguide (ref. 7). The focal-length measurements (ref. 7) indicate that the lens is aberration free up to about 90% of the aperture. Two waveguide geodesic lenses are used in the IOSA: one collimation lens and one Fourier transformation lens. Both lenses are identical, and their parameters are listed in Table 1. Since the aspherical lens profile has a smooth transition region that takes up 15% of the lens aperture, the useful lens aperture is 7.4 mm.

FABRICATION OF ASPHERICAL DEPRESSIONS

The fabrication of geodesic lenses involves two stages: grinding and polishing the lens depression with high precision. Ultrasonic impact grinding has been selected for both of these operations. The key problem appearing in the optical polishing is to obtain an optical surface without destroying the complex lens profile, in particular, the edge rounding region.

Ultrasonic impact grinding employs a tool bearing the shape of the designed depression. Ultrasonic energy transmitted through the tool agitates the abrasive slurry, and material is removed from the sample surface. The ultrasonic impact grinding technique is capable of replicating the tool shape within a 1/4-μm tolerance (ref. 6). The operation requires more than one tool to reduce the effects of tool wear.

Ultrasonic impact grinding is a complicated process governed by many parameters. We have empirically determined the optimum values of tool shapes, tool materials, grinding pressures, stroke amplitudes, workpiece materials, slurry speeds, abrasive concentrations, and grit sizes for our specific lens designs. Double lens pairs have been ground on 6.35 cm x 3.81 cm x 0.318 cm (x-z-y) $LiNbO_3$ substrates. After polishing and diffusion of Ti to form planar waveguides, we experimentally determine the location of the focal planes of the lenses and polish the edges to coincide with the focal planes.

LENS TOLERANCE ANALYSIS

Recently, Betts et al (ref. 8) published expressions for tracing rays in rotationally symmetric geodesic lenses. These expressions have been used to calculate the effects of tool wear, and lens depth.

The profile used in the calculations is for an f/1.5 lens. Some of the results of these calculations are given in Figures 7 and 8. Figure 7 shows the focal length increase, with percentage depth for both the tool wear analysis and the decrease in depth while maintaining the actual profile (surface removal).

For an f/1.5 lens, the diffraction-limited spot size is .58 μm at a wavelength of 0.8 μm in $LiNbO_3$. For a 1-cm-diam lens, this corresponds to 3×10^{-4} units in Figure 8. Hence, to maintain diffraction-limited performance, a depth change of $\sim$1% can be tolerated if 90% of the original useful aperture is used. For greater tool wear, a smaller aperture is required to maintain a diffraction-limited performance. This was experimentally demonstrated with a lens fabricated in $LiNbO_3$, where an 80 % aperture gave near-diffraction-limited performance.

From the experimental and calculated results, we concluded that in any system fabricated using geodesic lenses the precise location of the focal plane could only be determined after the lens fabrication. The focal position is very sensitive to fabrication tolerance, but the focal spot size remains diffraction limited within achievable fabrication tolerances.

SAW TRANSDUCER DEVELOPMENT

During this phase of the program we developed a 500-MHz bandwidth, 1-GHz operating frequency SAW transducer suitable for use in the IOSA, and we acoustically characterized the Ti:$LiNbO_3$ structure. Experiments were carried out to measure propagation loss, velocity dispersion, and acousto-optic deflection efficiency on various Ti:$LiNbO_3$ substrates. A modified chirp transducer (MCT) was able to achieve acousto-optic deflection bandwidths exceeding 400 MHz for both HeNe and GaAlAs laser wavelengths. This is the largest acousto-optic deflection bandwidth reported to date for a single transducer at either laser wavelength.

The MCT is similar to a conventional chirp transducer in that it has electrode spacings that vary smoothly from one end of the transducer to the other. This ensures that a portion of the transducer electrodes is synchronous at all frequencies within the passband. The chirp transducer response is relatively smooth over its bandwidth.

The total number of electrodes in the chirp transducer can be changed to facilitate impedance matching with virtually no effect on the shape of the output spectrum. In fact, the number of electrodes can be set so as to yield the ideal transducer loss with no external matching circuit whatsoever. In the case of the chirp transducer, each interelectrode gap has a characteristic ("instantaneous") synchronous frequency and it can be tilted to satisfy the Bragg condition at that frequency. Figure 9 shows the modified chirp transducer configuration with tilt angle varying smoothly over the transducer band. At any frequency within the band, a small number of electrodes are in quasi-synchronism, while contributions from the remaining electrodes add

in virtually random phase. For this reason, SAW generation is confined to a single "active" region that slides along the transducer as the drive frequency is changed. The number of excitation electrodes N_a comprising an "active" section for a linear FM chirp transducer is given by

$$N_a(f) = \frac{f}{f_o} \frac{N_{TOT}}{\sqrt{\Delta f \Delta \tau}} ,$$

where $N_{TOT} \cong 2f_o \Delta\tau$ is the total number of electrodes, f_o is the midband frequency, and $\Delta\tau$ is the transducer length divided by the SAW velocity. The total number of electrodes can be varied to satisfy convenient impedance-matching conditions. When the transducer aperture is fixed by acousto-optic interaction length considerations, N_{TOT} can be increased until the midband capacitive reactance reaches 50 Ω. At this point, the transducer can be coupled to a 50 Ω generator without any tuning. In addition, losses due to parasitic resistance in the metal film can be reduced by making N_a large, since the electrode resistance term is inversely proportional to the number of active electrodes.

The transducer pattern ultimately used in the development of the IOSA was a modified chirp transducer operating at 600 MHz with a 400-MHz bandwidth. This transducer, shown schematically in Figure 9, consists of 180 electrodes with N_a = 21 arranged in a two-track "dog-leg" structure to improve the impedance matching characteristics. The total aperture is 76 wavelengths, and the total tilt angle variation is 1:7°, since this design covers the frequency range from 350 to 900 MHz. The transducer photomask pattern with non-parallel electrodes was programmed on a computer-controlled optical plotter and photographically reduced in 3 stages. The devices were then built using contact optical photolithography. In all cases, the transducers were etched from 500-Å-thick aluminum metalizations.

PERFORMANCE

Data was obtained on acoustic conversion efficiency, propagation loss, velocity dispersion, and acousto-optic deflection efficiency.

The 600-MHz MCT pattern was initially fabricated on untreated yz $LiNbO_3$. Measurements were made of the insertion loss of this transducer in a non-dispersive delay-line configuration and are shown in Figure 10. The measured conversion efficiency agreed quite well with the theoretical value of 13 dB. The insertion loss varies from 14 dB at the lower edge of the band to 12 dB in the middle. Varying the length of the gold wire leads causes the passband to tilt by as much as 5 dB. Excellent agreement between the theoretical and the measured response was achieved.

Using test delay lines fabricated on Ti-diffused $LiNbO_3$ samples, measurements were made of acoustic propagation losses. The resulting data is shown in Table 2. To obtain this data, it was assumed that the measured insertion loss of the untreated samples consisted of the sum of the conversion efficiency and the theoretical propagation loss predicted by Szabo and Slobodnik (ref. 9).

There is great disparity in the propagation loss data obtained. An attempt was made to correlate the attenuation values with the temperature profiles used during the Ti diffusion. The times at each temperature are also shown in the table.

Sample N-92, which exhibited essentially theoretical propagation loss values, was heat treated at 650°C for 2 hours and at 950°C for 5 hours. The higher losses measured for sample N-95 indicate that the time at both 650°C and at 950° C are critical in determining the propagation loss of the samples.

The layered Ti:$LiNbO_3$ structure is expected to exhibit some acoustic velocity dispersion. It is important to characterize the amount of dispersion because the frequency dependence of the optical deflection angle δ and hence of the detector spacing is dependent on velocity.

The dispersion of the acoustic time delay was measured for crystals with differing diffusion temperature profiles. The results are given in Table 3. These results were obtained from a computer-controlled rf network analyzer that measured the insertion phase of a delay line consisting of two 600-MHz MCTs and performed a second-order least-squares fit. The values of 1.6×10^{-5}/MHz measured for these devices corresponds to a change in time delay of 0.64% for a 400-MHz bandwidth. However, of more importance is the error in position of the detector cells because they are uniformly spaced. The fractional position error of the high-frequency end of the detector can be calculated relative to the low-frequency end. The result is that for a 400-MHz bandwidth centered at 600 MHz, the error is 1%, or 1 detector cell width.

Acousto-optic deflection data was obtained for devices consisting of Ti:$LiNbO_3$ substrates with 600-MHz MCT transducers. The setup shown schematically in Figure 11 was found to be the most convenient and the most accurate method for obtaining this data. The light beam from the laser is coupled into the waveguide using a rutile prism coupler. The guided optical beam traverses the acoustic path, and the undeflected and deflected beams emerge from the waveguide at the edge of the crystal. There they are imaged on solid-state detectors using a cylindrical lens. The deflection efficiency is then determined by taking the ratio of the two optical intensities. The SAW transducer is driven by an rf oscillator and amplifier. The incident rf power can be monitored using a power meter. The primary advantage of this technique is that no output prism coupler is required. The main disadvantage of this technique is that a chip-free polished edge must be obtained on the output edge of the $LiNbO_3$ substrate. Otherwise, the light in the waveguide is scattered and cannot be properly imaged on the detectors.

Figures 12 and 13 show acousto-optic deflection efficiency versus frequency measured with 100 mW of rf power incident on the SAW transducer.

Figure 12 shows the response obtained using a GaAlAs double-heterojunction laser with a TE polarization, and with a wavelength of 0.83 μm. The 0 dB here corresponds to a 1.6% deflection efficiency; the transducer bandwidth is 420 MHz.

As proof of the effectiveness of the tilted fingers to steer the acoustic beam and affect the bandwidth, a measurement was made on the deflection coefficient when the laser was incident from the opposite side. This is equivalent to changing the sign of the direction in which the electrodes tilt. The result is a response that is significantly narrowband compared with that shown in Figure 12. Using Equation (15) (of Ref. 10), the shape of this response can be calculated; it is shown in Figure 13, along with the curve measured. The two curves agree quite well and the response is significantly narrowband relative to the parallel electrode case. The slight displacement in frequency between the two curves results from the experimental uncertainty concerning the frequency at which the Bragg condition was exactly satisfied.

DETECTOR ARRAY AND CCD READOUT

The detector array of the IOSA is designed to detect SAW deflected laser light, to provide information on incoming rf frequency, and to read out with a charge-coupled-device shift register.

The CRC 139 detector array is made of a single row of 100 silicon MOS photodetectors and 4 output CCD shift registers located on both sides of the detectors. These small photodetectors are made of MOS capacitors with semi-transparent polysilicon gates. The CCD shift register is fabricated using polysilicon gate buried-channel CCD technology to reduce noise and increase the rate of charge transfer. The CCD is fabricated with n-channel CCD technology to take advantage of higher electron mobility. The schematic cross section of a buried p-channel MOS photodetector compatible with the above n-channel CCD technology is shown in Figure 14.

When a bias voltage is applied on the gate of the MOS capacitor, a depletion region is formed under the polysilicon gate. Electron-hole pairs generated by photons penetrating the silicon substrate will be separated by the electric field in the depletion region. The electrons collected at the $Si-SiO_2$ interface become the signal charge.

The primary performance goals of the detector array were:

- An rf frequency resolution of 4 MHz
- A dynamic range of 40 dB
- A total sampling time of <3 μsec.

The detector cell width S is constrained by the required rf frequency resolution and by the allowed optical crosstalk between adjacent cells discussed earlier. Using the parameters associated with Figure 3, the detector cell width defined by frequency resolution requirements is $S \leq 4.26 \times 10^{-4}F$, and the cell width defined by optical resolution requirement is $S \geq 1.32 \times 10^{-4}F$. A small focal length F corresponds to a small detector size. The detector width, however, is restricted in the lower limit by detector-CCD fabrication and coupling considerations, and by dynamic range requirements. The detector coupled to CCD shift registers is shown in Figure 15. To facilitate the charge transfer, it is desirable to have equal width for both the detector and the CCD cell. It is difficult to make the width smaller than 16 μm per bit or 8 μm per detector for a 2 detector to 1 bit dual multiplexer. There are channel stops between the detector cells to isolate the cells from one other. The minimum channel stop width that can be made on a mask is 1.5 μm and will be 3.5 μm wide after processing. With a spot size of about 2.5 μm, the detector size should be at least 7 μm to contain the full light spot. To satisfy the dynamic range requirement of 40 dB requires a rather large detector storage area. Any further reduction in detector width will make the detector length even longer and slow down charge transfer. Based on these considerations, we chose a detector width of 8 μm for the Fourier transform lens with a focal length of 1.88 cm. This gives the required frequency resolution of 4 MHz.

A dynamic range of 40 dB is required for system applications. The dynamic range is defined as the range between detector saturation due to strong signal and the overall noise level. The determination of expected noise level is, therefore, very important for designing the full charge capacity of both the detector and CCD unit cells.

The usual noise sources of a detector/CCD array can be separated into three categories: those associated with the input, the integration and transfer, and with the output. These noise effects are listed in Table 4 with special emphasis given to the comparison of noise characteristics of surface- and buried-channel CCDs.

The conclusion that the noise level of a surface-channel CCD is about four times higher than that of a buried-channel CCD has led to the selection of the buried channel device for this program. To achieve a dynamic range of 40 dB, or 10^4 to 1, the charge capacity of both the detector and the CCD storage well must be at least 10^4 times greater than the noise level. The noise level of a buried-channel CCD and its output amplifier is about 210 electrons. A full charge capacity of 6×10^6 electrons is thus designed for this array. Assuming a charge density of 1×10^{12} electrons/cm^2, this results in a detector of

$$\frac{6 \times 10^6 \text{ electrons}}{1 \times 10^{12} \text{ electrons/cm}^2} = 6 \times 10^{-6} \text{ cm}^2 .$$

With an effective detector width of 4.5 μm, this requires a detector length of at least

$$\frac{(6 \times 10^{-6} \text{ cm}^2)}{(4.5 \times 10^{-4} \text{ cm})} = 1.33 \times 10^{-2} \text{ cm} = 133 \text{ μm} .$$

Therefore, the detector size is designed to be 8 μm by 150 μm.

The 100 detectors should be sampled as fast as possible, preferably within 3 μsec. Therefore, the detector, the CCD shift register, and the output amplifier are all required to have high-speed operation. Three basic mechanisms are responsible for carrier transfer in a CCD: thermal diffusion, self-induced drift, and fringing fields. A summary showing thermal diffusion time constants, fringing field, and carrier mobility is shown in Table 5. An epi concentration of 5×10^{14}/cm^3 (30 Ω-cm) and a potential difference of 10 V between adjacent electrodes are assumed. Also listed in Table 5 are t_4, the time to achieve a transfer efficiency of four 9's or 0.9999, and f, the maximum operating frequency assuming a 2-phase clocking.

With a readout scheme as shown in Figure 15, each of the CCD registers will have a maximum of 100 transfers between detector and output amplifier. If a 3-μsec sampling time is desired, a transfer time t_4 of less than 3×10^{-8} sec would be required. Table 5 shows that CCDs with an electrode length of 7.5 μm or less have a very good chance of meeting this goal. The electrode length chosen in the present design is 6 μm.

IOSA DEVICE TESTING AND PERFORMANCE

The IOSA is a complex device and extensive testing is needed for performance evaluation. Looking at the close-up of a fully assembled IOSA in Figure 16 we can clearly discern the detector/CCD chip at the top end, the two geodesic lenses in the middle, and the semiconductor laser at the lower end of the $LiNbO_3$ integrated optic chip. Two sets of SAW transducers can be seen in the middle of the $LiNbO_3$ chip on

either side of the axis of the crystal. The significant features of the IOSA's performance are:

- Acousto-optic bandwidth
- Single-tone rf resolution
- Single-tone dynamic range
- Two-tone rf resolution
- rf pulse measurements.

Acousto-Optic Bandwidth

The IOSA device depends on acousto-optic Bragg deflection for its successful operation. The bandwidth associated with the acousto-optic interaction depends on the rf bandwidth of the transducer for efficient SAW generation, as well as k-vector matching of the optical and surface acoustic waves. But a purely rf characterization of the transducer reveals only a part of the picture. In order to evaluate the acousto-optic response we make use of an experimental arrangement, illustrated by the schematic in Figure 17. To obtain the optimum acousto-optic response we need to arrive at the correct position for the semiconductor laser. This is decided by measuring the acousto-optic response corresponding to different transverse positions of the semiconductor laser with respect to the axis of the collimating lens. In this measurement a 1 kHz amplitude modulated rf signal is amplified and applied to the SAW transducer of the IOSA. The directional coupler between the rf amplifier and the SAW transducer facilitates measurement of the incident and reflected rf power levels. The deflected optical spot at the output edge of the crystal is imaged onto a photomultiplier. The beam splitter arrangement allows monitoring of the output edge of the crystal on a video monitor. The signal from the photomultiplier, together with the 1 kHz modulating signal from the wavetek oscillator, is fed to the signal and reference channels of a PAR 124A lock-in amplifier. The analog output from the lock-in is used to drive an XY-plotter. Because of the lock-in measurement technique employed, any scattered light from the substrate does not cause problems. With this experimental arrangement we have been able to rapidly measure the acousto-optic bandwidth for each position of the semiconductor laser.

The optimum acousto-optic response, measured with an HLP 1400 laser coupled to the IOSA chip, is shown in Figure 18. The 3 dB bandwidth is $\sim$380 MHz. The acousto-optic deflection efficiency corresponding to the 0 dB level at a frequency of 615 MHz and 100 mW, was measured as the ratio of the deflected spot signal to the undeflected spot signal. The deflected spot signal was arrived at by substrating out the signal due to any scattered background. For the two samples tested we have observed efficiencies of 0.83% (sample 4 with HLP 3400 U laser), and 0.97% (sample 3 with HLP 1400 CSP laser), respectively. The irregular structure observed in the acousto-optic response of Figure 18 is due to rf mismatch which arises from the coaxial cable (RG57, BNC) between the output of the directional coupler and the SAW transducer. This has been checked by monitoring the reflected power, keeping the incident power at a fixed value of P_{avg} $\sim$100 mW, and measuring the acousto-optic response over the frequency range 400 MHz to 900 MHz. In Figure 19 we have plotted the acousto-optic response, as well as the net rf power flowing into the SAW

transducer/coaxial cable pair versus frequency. The correspondence between the peaks and valleys of the acousto-optic deflection efficiency with the peaks and valleys of the net power into the SAW transducer confirms this conclusion.

Single-Tone RF Resolution

The IOSA device was designed to have an acousto-optic 3 dB bandwidth of 400 MHz, with a center frequency of 600 MHz and a single-tone resolution of 4 MHz. Acousto-optic response measurements discussed earlier indicate that the Bragg cell design does indeed yield a 3 dB response of $\sim$380 MHz, very close to the $\gtrsim$ 400 MHz rf bandwidth. The single-tone resolution of the device depends on a number of factors such as the gap between the laser emission facet and the input end of the $LiNbO_3$ crystal, the positions of the focal planes of the collimating and Fourier transforming lenses with respect to the edges of the $LiNbO_3$ crystal, SAW transducer alignment, and the distance between the output end of the $LiNbO_3$ crystal and the surface of the detector/CCD chip.

Even though the acousto-optic response was less than optimum, single-tone frequency measurements performed on the device are nevertheless interesting.

A single-tone measurement carried with a 725 MHz 100 mW rf signal is shown in Figure 20. The detector/CCD chip is organized in a way that data is read out in two channels as strings of 50 pixels each. In order to determine the frequency resolution we need to have data from both the output channels properly interleaved on the display. The photograph in Figure 20 shows output of all the 100 pixels in proper time sequence. The upper photograph is an oscilloscope trace of the 100 detector/CCD array. Referring to Figure 20, the straight horizontal part of the trace on the left-hand side defines the zero signal level. The pedestal seen in all of the other pixels in Figure 20 is due to in-plane scattered light. The pixel corresponding to the rf signal of 725 MHz has been highlighted. The adjacent cells that are 4 MHz away by design exhibit a signal half as strong as the pixel corresponding to the peak. The 3 dB frequency resolution is therefore 8 MHz. The lower half of Figure 20 illustrates the display on a regular electronic spectrum analyzer when the same 725 MHz rf signal is incident on it. As a second example, the photograph in the upper part of Figure 21 illustrates the output from one half of the detector/CCD array when a 705 MHz, 100 mW rf signal is incident on the SAW transducer of the IOSA. Once again, the lower part is the display of a conventional spectrum analyzer with the same 705 MHz, 100 mW rf signal incident on it.

Single-Tone Dynamic Range

The dynamic range of response is an important parameter in the evaluation of the IOSA. As outlined earlier, in-plane scattered light appearing at the output of the $LiNbO_3$ crystal results in a fixed pattern of noise impinging on the detector/CCD array. The resulting pedestal of background light is clearly illustrated in Figure 20. Dynamic range measurements were carried out with respect to the fixed background pattern. Measurements were carried out without resorting to a lock-in type of phase sensitive detection. With the output of the detector/CCD chip displayed on an oscilloscope, we read signals off the screen corresponding to each value of the rf drive signal. Also, to get an estimate of the cross-talk figure for our device, we measured the signal appearing in a pixel which was next to the nearest neighbor, corresponding to a frequency gap of 8 MHz. The result of one such

measurement is shown in Figure 22. The detector/CCD clocking was carried out at 333 kHz, with the rf at 729 MHz and an I_{laser} = 21 mA. The signal in the main pixel saturates for rf power greater than about 200 mW, resulting in a dynamic range of 20 to 23 dB, with the minimum visually discernable signal level at about 1 mW (rf). The receiver sensitivity for the IOSA as determined by observing the detector/CCD output on an oscilloscope would be 1 mW (of rf power). The signal in the next to nearest neighbor (8 MHz array) appears to be a factor of 4 smaller than the main pixel. This measurement is again in agreement with our 3 dB resolution figure of 8 MHz (Figure 20).

The dynamic range is currently limited by saturation of the detector at the high signal end, and by the presence of the fixed pattern background signal at the lower end. Steps such as improved crystal handling, improved waveguide fabrication, and polishing of the crystal surface after waveguide formation can be pursued to reduce in-plane scattering of light.

Two-Tone RF Resolution

Functionally, the IOSA is expected to receive and analyze multiple rf signals for their frequency and amplitude characteristics. An important parameter in analyzing more than one rf component at a time is the minimum spacing between adjacent signals below which the device fails to resolve. The two-tone resolution measurement attempts to quantify the device performance in regard to simultaneous multiple signal spectral analysis. In this device design, the spacing between adjacent detector pixels corresponds to an rf increment of 4 MHz. If the achieved rf resolution were such that a significant response was observed in detector pixels adjacent to the intended pixel, two-tone resolution would suffer. Single-tone resolution measurements discussed earlier (see Figure 20) have shown that the strength of the signal in an adjacent detector pixel 4 MHz away is only a factor of 2 smaller. Assuming a simple Gaussian spot shape impinging on a detector element, we would not expect the device to resolve a pair of adjacent rf signals of equal strength and 8 MHz separation. Yet our measurements with the device indicate that a pair of equal strength rf signals 8 MHz apart are resolved. Oscilloscope displays of the output of the detector/CCD chip, when the SAW transducer is driven by two rf signals of 100 mW intensity separated by 8 MHz, is illustrated in Figure 23. In Figure 23(a) the output of the 100 element detector/CCD chip is shown in proper time sequence. In Figure 23(b) the outputs from the two shift registers are displayed separately. The rf spacing between adjacent points in Figure 23(b) is 8 MHz, while the spacing between adjacent points in Figure 23(a) is 4 MHz. In Figure 23(c) and (d) we show time expanded details of the displays in parts (a) and (b). The rf spectrum of the signal used to generate the output in Figure 23(a) is shown in Figure 23(e). The central signal at 689 MHz is 20 dB smaller than its two neighbors at 685 MHz and 693 MHz, respectively. Hence, the full 200 mW of rf power is distributed equally between the two signals at 685 MHz and 693 MHz. An examination of the display in Figure 23(a) shows that the pixel corresponding to 689 MHz exhibits a response 0.7 dB below the pixels at 685 MHz and 693 MHz. Thus, two equal strength signals separated by 8 MHz are clearly resolved.

In order to characterize the two-tone resolution of the device, we carried out a number of other measurements. Similar displays were obtained when the spacings between the two 100 mW rf signals were 12 MHz, 16 MHz, 24 MHz, and 40 MHz, respectively. Resolution of the two rf signals in each case was very clear, as shown in Figure 24,with a frequency offset of 12 MHz.

An interesting feature of the two-tone measurement is concerned with the measurement of the dynamic range of a signal in the presence of a strong signal nearby. Referring to Figure 20, we find it necessary to move 20 MHz (5 or 6 adjacent detector pixels) to achieve a cross figure of -20 dB. This means that in the presence of a strong signal, a weak signal would not be clearly resolved (with a cross-talk figure of -20 dB) unless it were $\geq$ 20 MHz away. The two-tone dynamic range is expected (if $\Delta f \geq$ 20 MHz) to be better than 10 dB for the weak signal. In order to improve the two-tone dynamic range we would need to improve the frequency resolution.

rf Pulse Measurements

The IOSA device is expected to receive and analyze rf pulses of short time duration. If a laser with a divergence angle of 11.45° is used with this optical system (with a focal length of 20 mm), it generates a collimated optical beam 4 mm wide. Combining the 4 mm optical beam width with a surface wave velocity of 3.5×10^5 cm/sec yields an acoustic aperture of 1.15 μsec. At any given instant in time the acousto-optic interaction can only analyze an acoustic wave train that is 1.15 μsec long. Because of the integrating nature of the detector/CCD chip, all light impinging on a given detector pixel during one integration period contributes to the signal packet. An acoustic aperture of 1.15 μsec corresponds to a frequency resolution of 0.85 MHz, and there does not appear to be an advantage in integrating signals for periods longer than the acoustic aperture. For analyzing pulses, it would be advantageous to carry out the signal integration process for the duration of one acoustic aperture. As the integration time is reduced, one must increase the power output of the semiconductor laser by a proportionate amount in order to maintain the large signal handling capacity of the device. At the same time, laser power scaling has a definite upper limit due to the limited power output (10 to 15 mW) of single mode semiconductor lasers.

With the present device we have operated the detector/CCD chip at a clocking frequency of 333 kHz, with an integration time of 192 μsec. With a laser power output of 1.5 mW and a total insertion loss of 17 dB from the laser facet to the output of the crystal, signal saturation appeared at rf drive power levels of 200 mW. We have carried out a set of calculations to arrive at different sets of operation alternatives for our IOSA. The results are summarized in Table 6. The last row in Table 6 indicates that with a 15 mW laser output and an integration time of 0.96 μsec, signal saturation should occur at an rf power level of 1000 mW. These are all numbers that appear reachable at this time.

To highlight some of the above issues, we present rf pulse measurement data in Figure 25 for the case when the integration time was 38 μsec (CCD clocking frequency of 1.67 MHz) and pulses of various duration were applied to the SAW transducer successively. The pulse widths were 38 μsec, 19 μsec, 15.2 μsec, 11.4 μsec, 7.6 μsec, and 3.8 μsec. The rf (710 MHz) power level was set at 100 mW under cw conditions, and the modulating signal's pulsewidth was varied to achieve the different duty factors. The signal level is reduced successively in direct proportion to the duty factor, as shown in the displays in Figure 25(a) through (f). For purposes of establishing the background level, we show the detector/CCD output in Figure 25(g) with no rf power applied to the transducer. Finally, in Figure 25(h) we have included the spectrum of the modulated signal (duty factor 0.2) as seen on a regular electronic spectrum analyzer. The displays in Figure 25(a) through (g) highlight the problems involved in analyzing rf pulses that are small fractions of the detector/CCD integration times.

CONCLUDING REMARKS

The results of measurements made on an integrated optic rf spectrum analyzer are reported. The performance of the device acousto-optic bandwidth, single-tone rf resolution, two-tone rf resolution, single-tone dynamic range, two-tone dynamic range, and single-tone rf response are presented. The device parameters that control device performance are analyzed. These results demonstrate the viability of the IOSA for real time spectrum analysis of pulsed and cw rf signals.

Improvements of rf bandwidth resolution can be obtained by the use of larger collimated optical beams. This requires larger optical lens elements, and hence, larger crystals.

REFERENCES

1. M.K. Hamilton, D.A. Willie, and W.J. Miceli, "An Integrated Optical RF spectrum Analyzer," Proc. IEEE 1976 Ultrasonic Symp. Annapolis, MD.

2. M.K. Barnoski, B. Chen, T.R. Joseph, J.Y. Lee, and O.G. Ramer, "An Integrated Optic Spectrum Analyzer," IEEE Trans. on Circuits and Systems, CAS-26, 1113-1124 (Dec, 1979).

3. R.D. Weglein, M.E. Pedinoff, and H. Winston, "Diffraction Spreading of Surface Wave on $LiNbO_3$," Electron Lett. 6, 20 (1970).

4. R.V. Schmidt and I.T. Kaminow, "Metal-Diffused Optical Waveguide in $LiNbO_3$," Appl. Phys. Lett. 25, 458-460 (1974).

5. D. Kassai and E. Marom, "Aberration-Corrected Rounded-Edge Geodesic Lenses," J. Opt. Soc. Am. 69, 1242-1247 (1979).

6. B. Chen, E. Marom, and R.J. Morrison, "Diffraction Limited Geodesic Lens for Integrated Optic Circuits," Appl. Phys. Lett. 33, 511-513 (Sept., 1978).

7. B. Chen and O.G. Ramer, "Diffraction Limited Geodesic Lens for Integrated Optic Circuits," IEEE J. Quantum Electron, QE-15, 853-860 (1979).

8. G.E. Betts, J.C. Bradley, G.E. Marx, D.C. Schakest, and H.A. Trenchard, "Axially Symmetric Geodesic Lenses," Appl. Opt. 17, 2346-2351 (Aug., 1978).

9. T. Szabo and A. Slobodnik, "The Effect of Diffraction in the Design of Acoustic Surface Wave Devices," IEEE Trans. on Sonics and Ultrasonics SU-20, No. 3 (July, 1973).

10. I.C. Chang, "Acoustooptic Devices and Applications" IEEE Trans. on Sonics and Ultrasonics SU-23, 2, (January, 1976).

Table 1. Parameters of Collimation and Fourier Transform Lenses.

Focal length	18.8 mm
Diameter	8.7 mm
Depth at center	1.1 mm
Useful aperture	7.4 mm
f/no.	2.54

Table 2. Measured Attenuation Values for Titanium Diffusion $LiNbO_3$, obtained at 600 MHz and 1000 MHz.

Sample Number	Oxidation Time at 650°C, hr	Diffusion Time at 950°C, hr	Attenuation, dB/μsec
			600 MHz
N-90	0	5	1.9
N-91	0	8	7.0
N-92	2	5	0.54
N-95	4	6	1.9
Untreated surface (theoretical)	0	0	0.43

Table 3. Measured Velocity Dispersion Coefficients for Ti:$LiNbO_3$ Substrates. Data Was Taken Over the 400 to 800 MHz Range.

Sample	Oxidation Time at 600°C, hr	Diffusion Time at 1000°C, hr	$d\tau = \frac{1}{\tau}\left(\frac{d\tau}{df}\right)$, 10^{-5} MHz or $\frac{-1}{V_s}\left(\frac{dV_s}{df}\right)$
A	4	5	-1.59
B	0	5	-1.78
C	4	5	-1.57
D	0	5	-1.59
E	4	6	-1.55
F	4	6	-1.45
G	4	6	-1.57
H	4	6	-1.75

Table 4. Noise Characteristics of Surface-Channel and Buried-Channel CCDs.

Operation	Process	Surface Channel	Buried Channel
Input	Fat zero input	178	0
Integration and transfer	Fast interface states	834	0
	Bulk states	∿0	90
	Dark current	<100	<100
Output	Reset amplifier	147	147
	MOSFET	68	68
Total noise electrons (rms)	All	873	210

Table 5. Charge Transfer Characteristics.

Carrier Mobility, $cm^2/V\text{-}sec$	Electrode Length, μm	t_{th}, sec	t_{tr}, sec	t_4, sec	f, MHz
600	10	2.56×10^{-8}	9.67×10^{-9}	6.6×10^{-8}	7.5
600	7.5	1.44×10^{-8}	3.04×10^{-9}	3.35×10^{-8}	14.9
600	6	9.23×10^{-9}	1.29×10^{-9}	2.04×10^{-8}	24.5
1000	10	1.54×10^{-8}	5.80×10^{-9}	3.97×10^{-8}	12.5
1000	7.5	8.65×10^{-9}	1.83×10^{-9}	2.01×10^{-8}	24.8
1000	6	5.54×10^{-9}	7.76×10^{-10}	1.23×10^{-8}	40.6

Table 6. Scaling of Laser Power and CCD Clocking to Maintain Performance.

Laser Power Output, mW	Total In/Out Insertion Loss, dB	Output Zeroth Order Power, μW	RF Power at Saturation, mW	Integration Time, μsec
1-5	17	30	200	19.2
15	17	300	200	19.2
15	11	1200	200	4.8
15	11	1200	1000	0.96

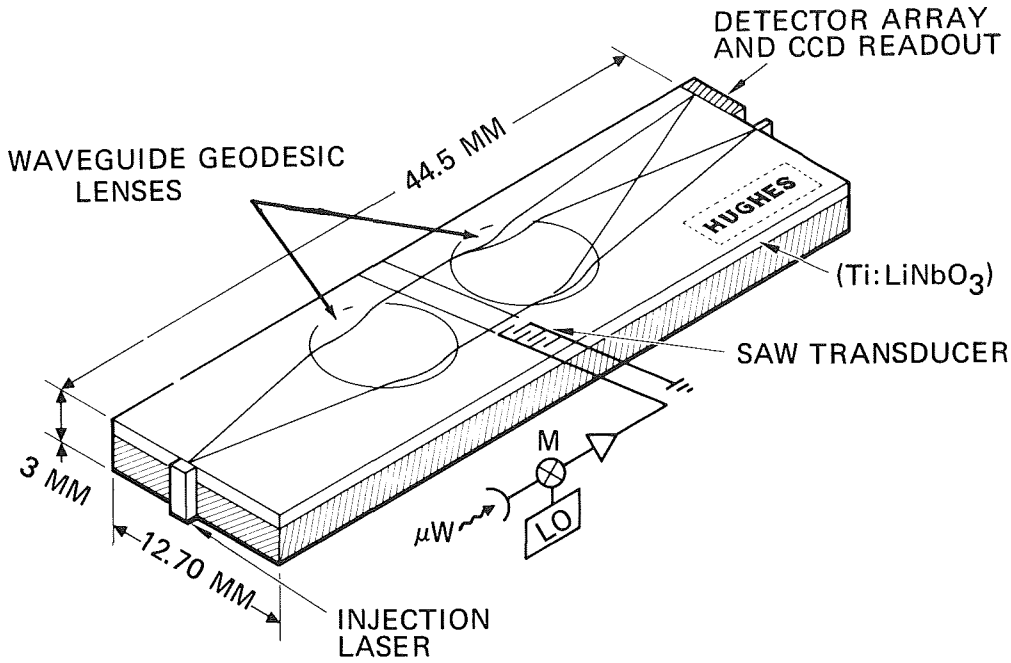

Figure 1.- Schematic of an integrated-optic spectrum analyzer.

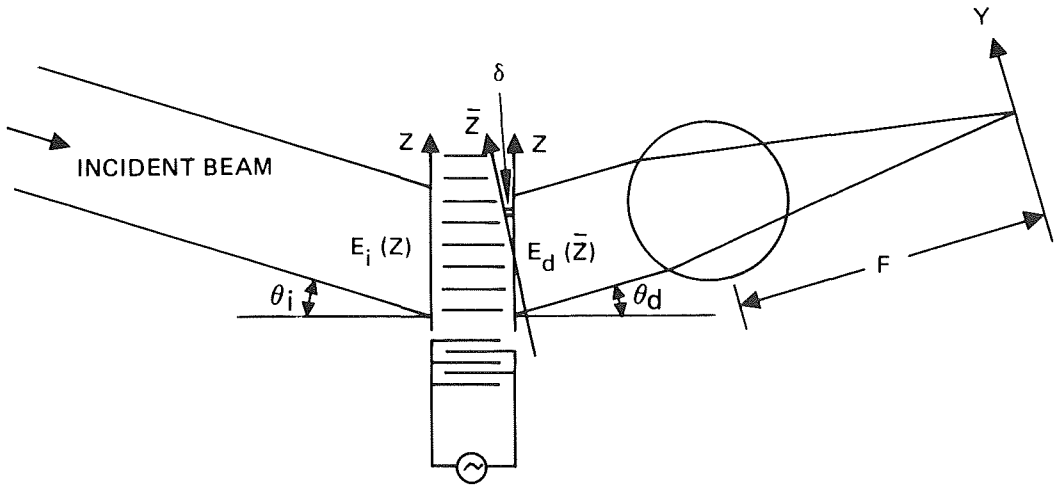

Figure 2.- Optical wavefront propagation through the acousto-optic interaction region and the transform lens.

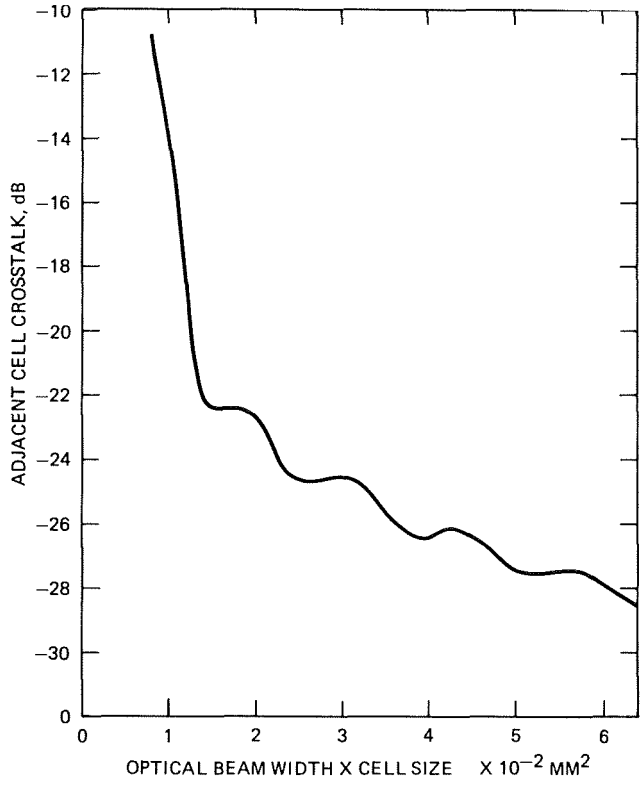

Figure 3.- Optical crosstalk in the adjacent cell of the detector array as a function of optical beam width and detector cell size.

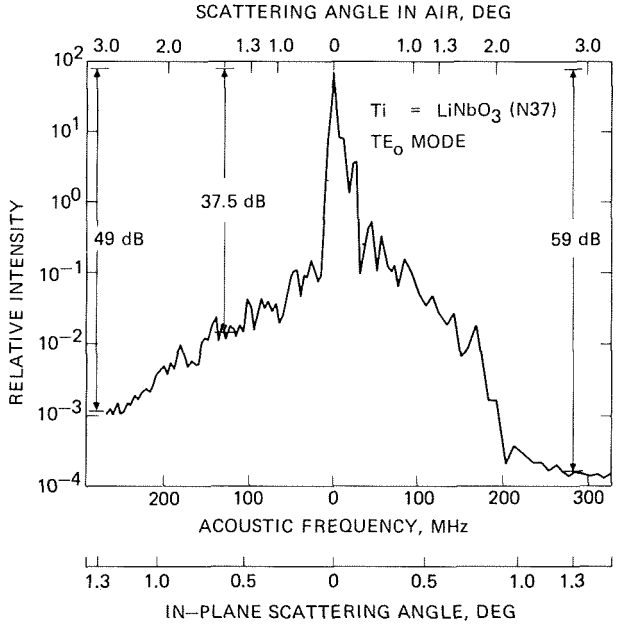

Figure 4.- In-plane scattering measurement of Ti:$LiNbO_3$ waveguide.

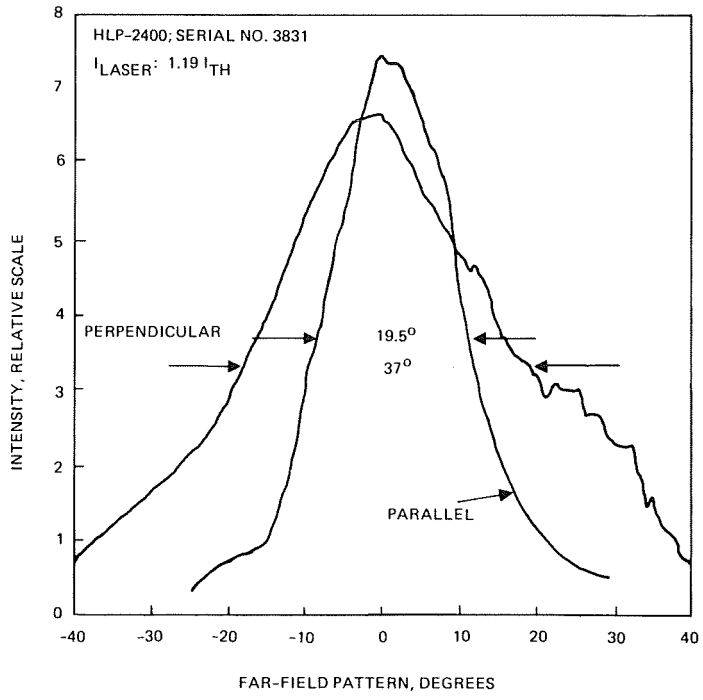

Figure 5.- Far field intensity pattern for a Hitachi HLP-2400 laser, Serial No. 3831.

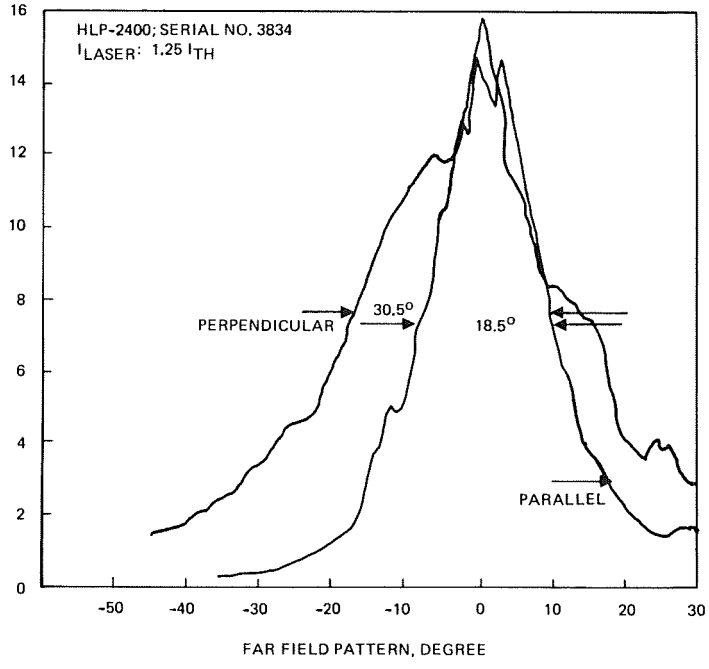

Figure 6.- Far field intensity pattern for a Hitachi HLP-2400 laser, Serial No. 3834.

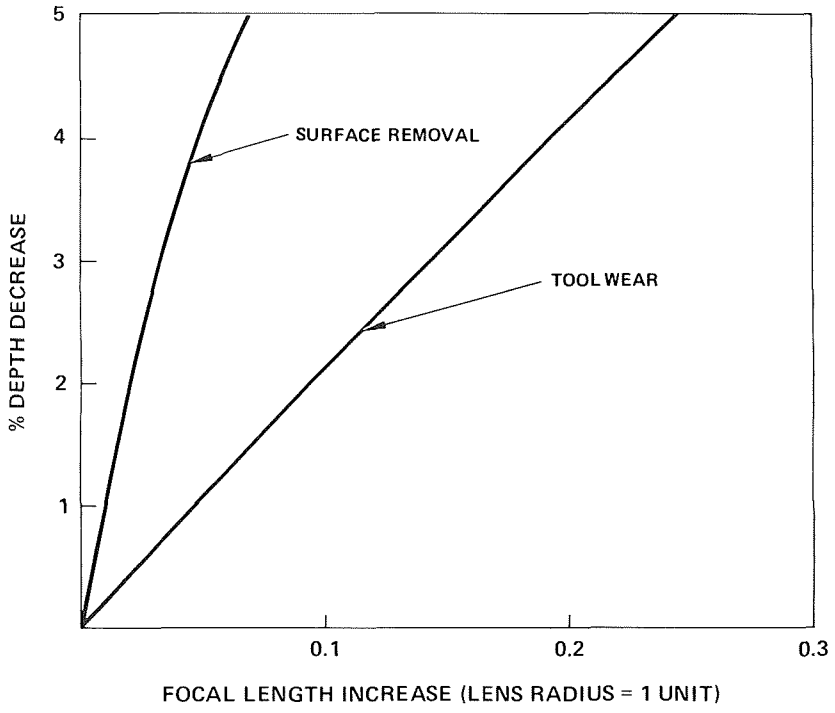

Figure 7.- Focal length increase versus percentage of depth decrease for both tool wear and surface removal.

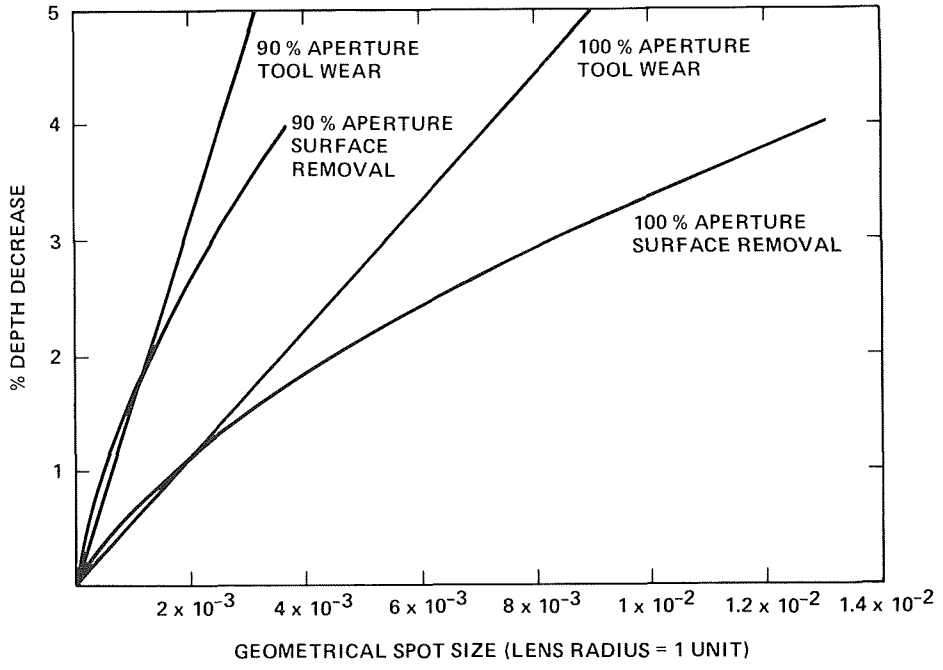

Figure 8.- Geometrical spot size versus percentage of depth decrease for both tool wear and surface removal. Two curves are provided for each one corresponding to 100% and 90% of the original useful aperture.

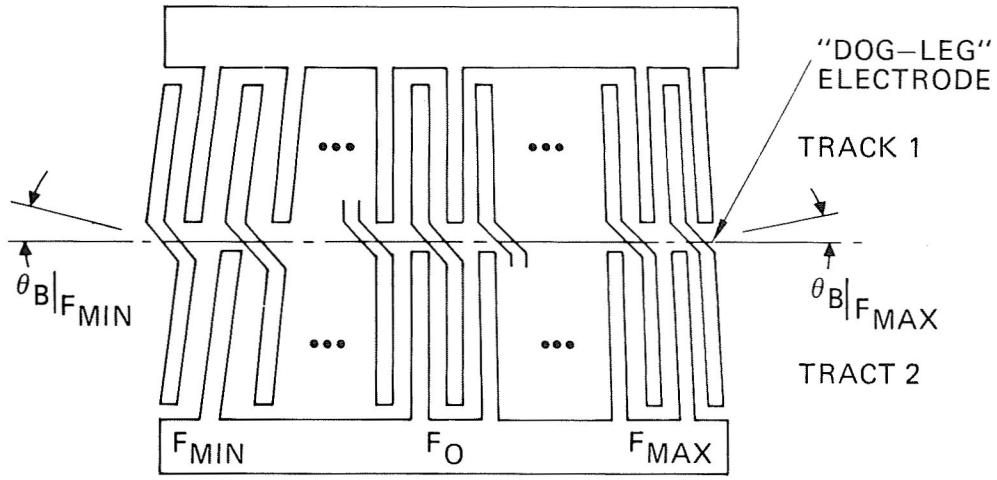

Figure 9.- Schematic of a modified chirp transducer with a two-track dog-leg electrode geometry.

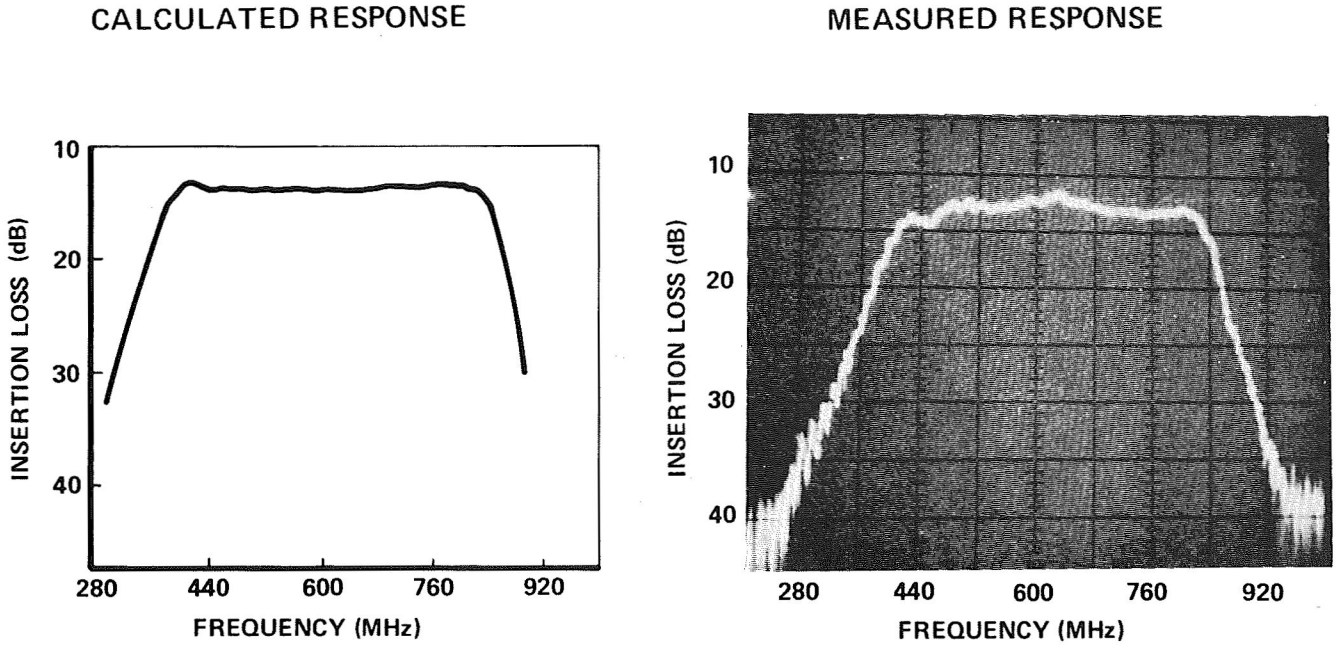

Figure 10.- Comparison between the calculated and measured responses of the 600-MHz modified chirp transducer.

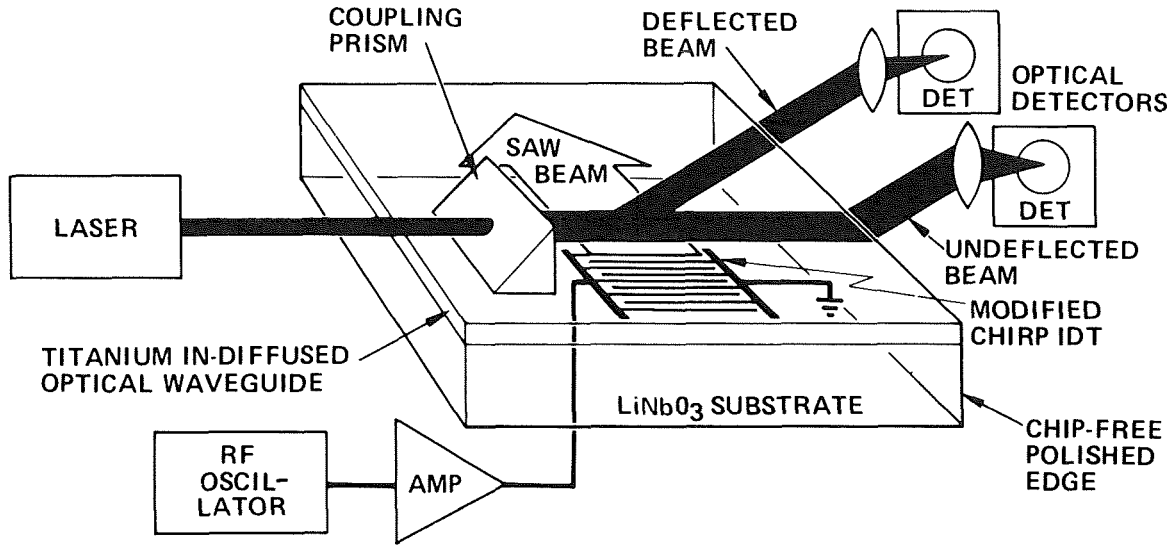

Figure 11.- Test configuration used in the measurement of the Bragg acousto-optic deflection coefficient.

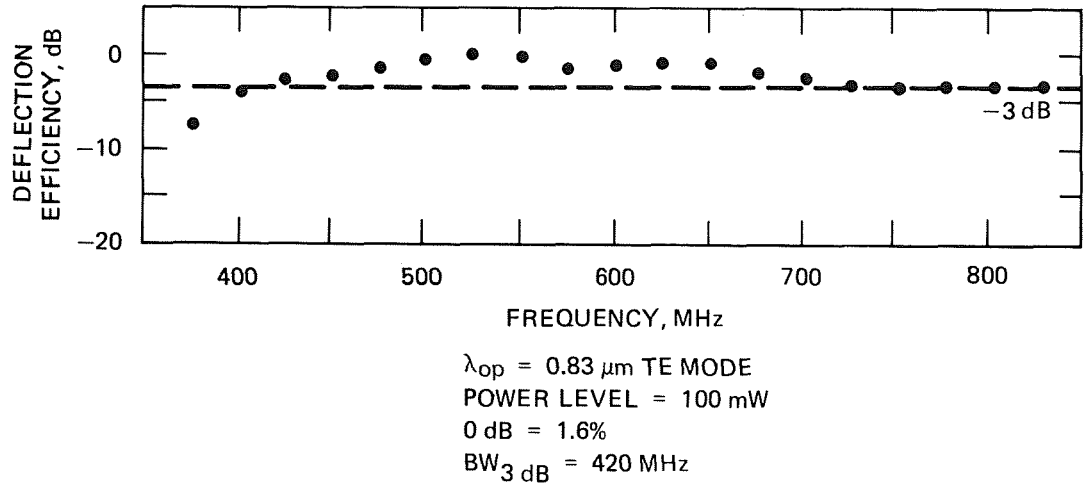

Figure 12.- Measured acousto-optic deflection efficiency for a TE-mode GaAlAs laser.

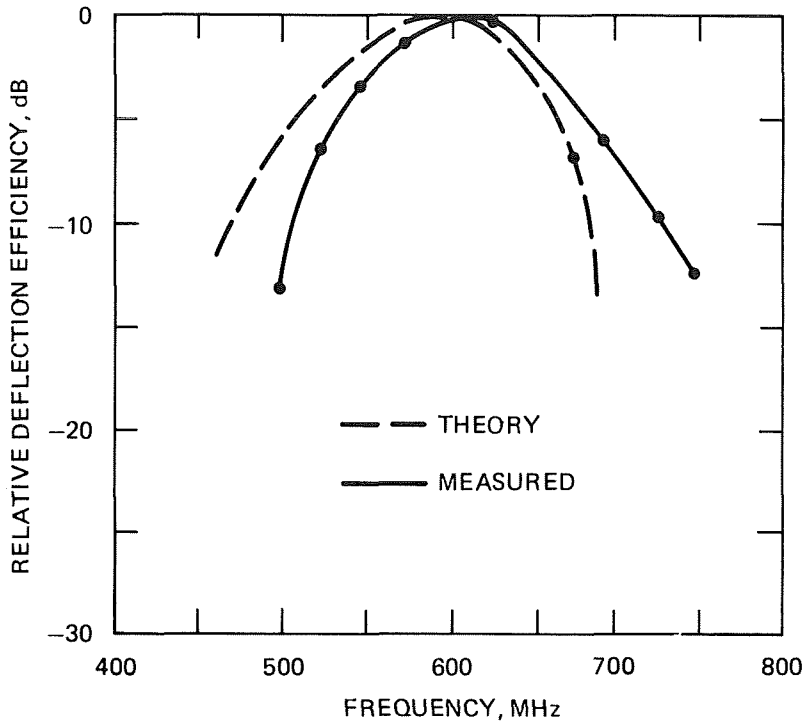

Figure 13.- Comparison of the theoretical and measured acousto-optic deflection efficiency when the sign of the electrode tilt is reversed.

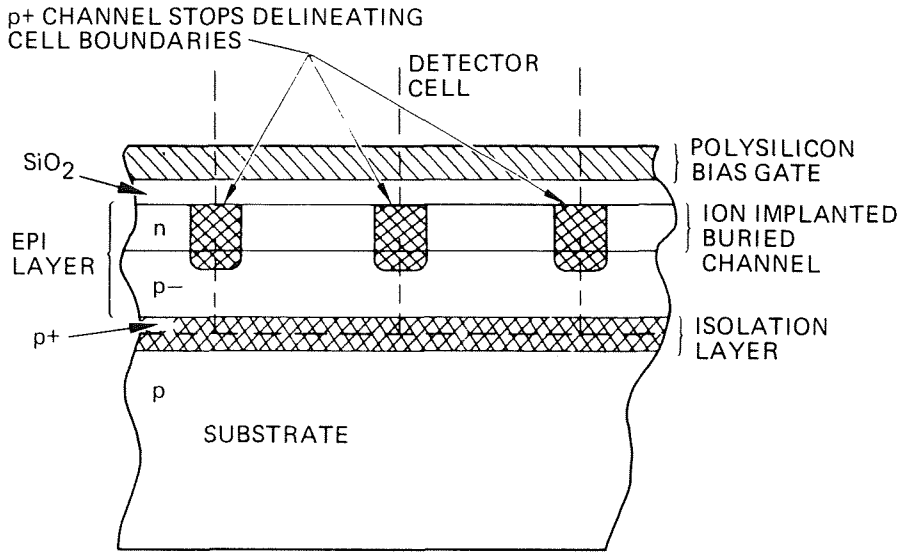

Figure 14.- Cross section of buried p-channel MOS photodetector.

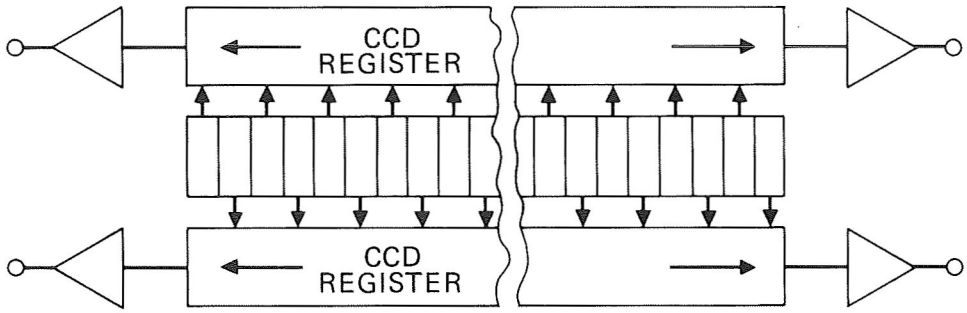

Figure 15.- Schematic showing detector array, CCD output register, and MOS output amplifiers. Arrows denote direction of charge transfer.

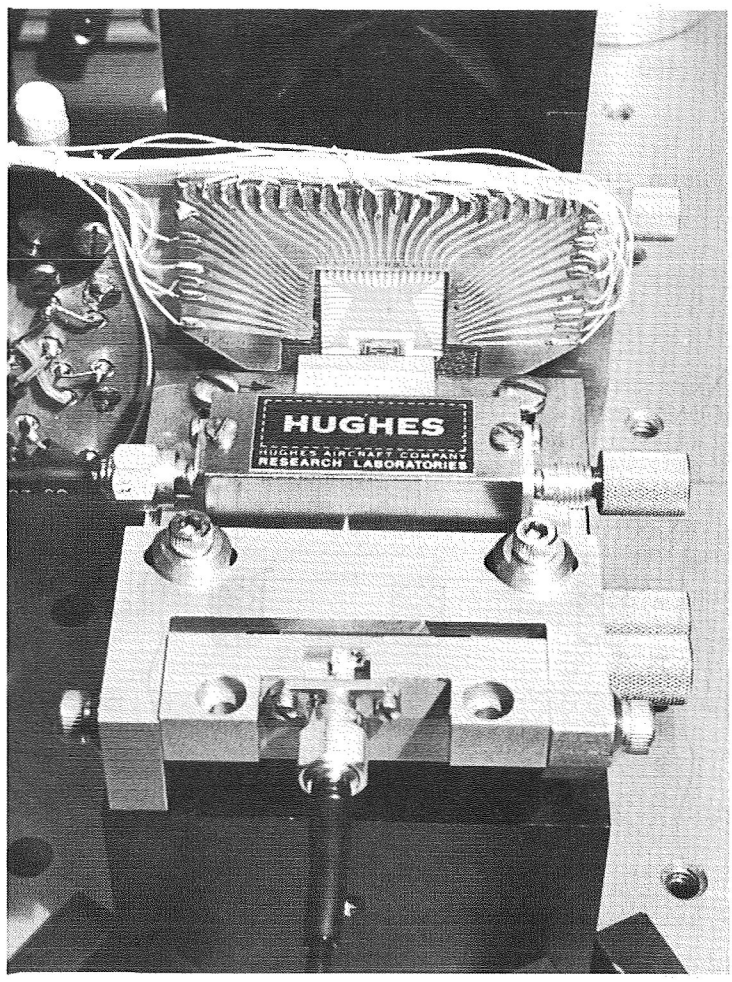

Figure 16.- Close-up photoghaph of the assembled IOSA.

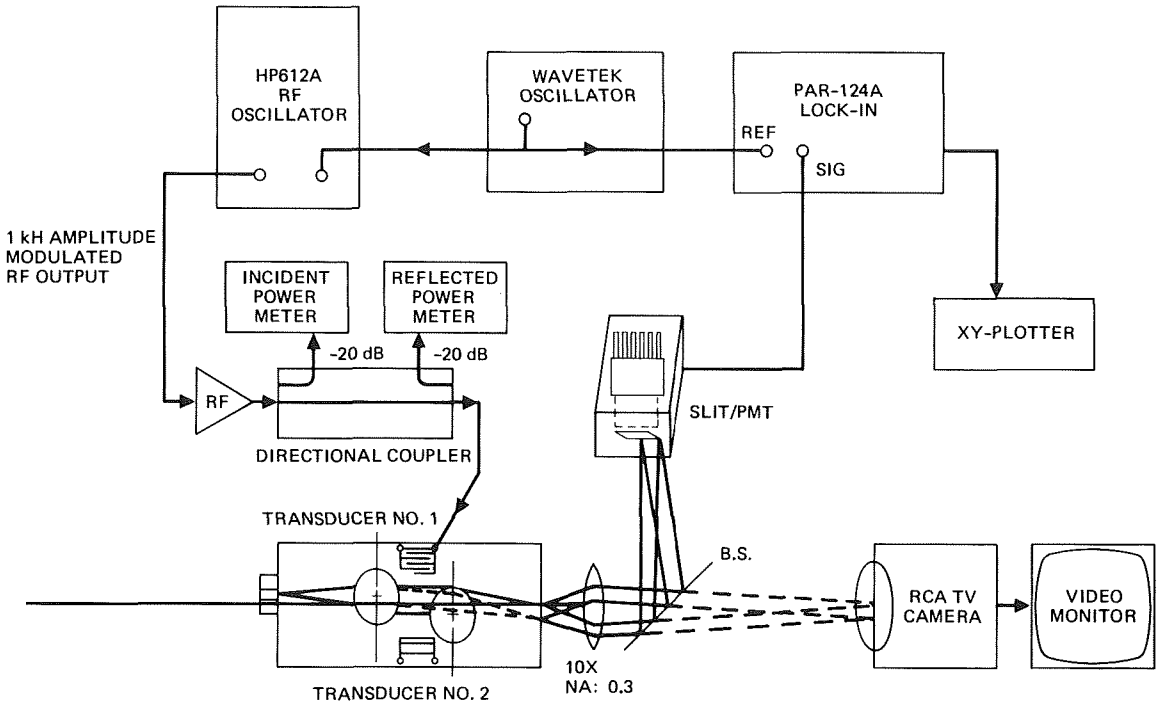

Figure 17.- Schematic of arrangement used to measure the acousto-optic response of the IOSA.

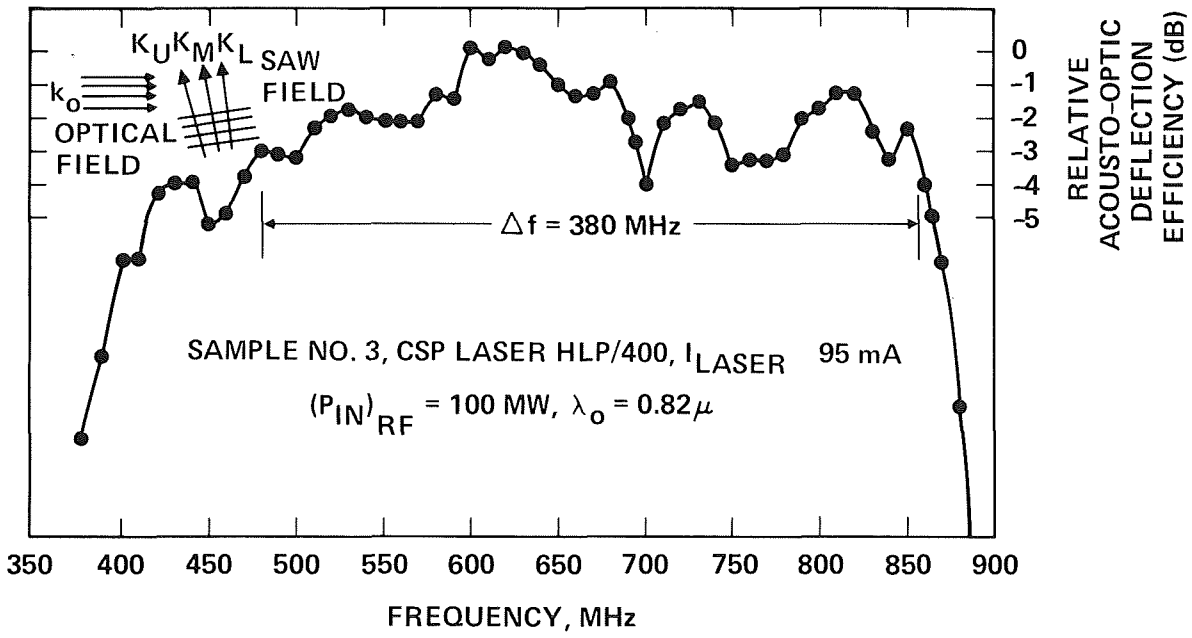

Figure 18.- Acousto-optic response measured on a device with a Hitachi HLP 1400 CSP laser.

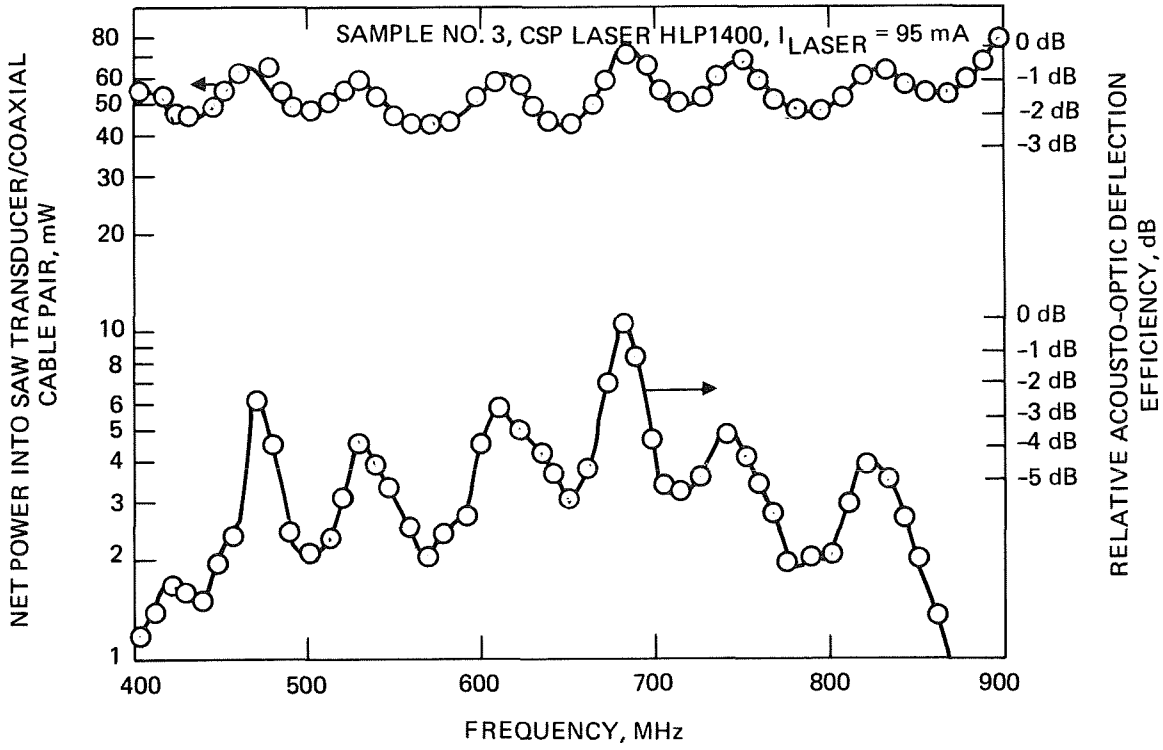

Figure 19.- Acousto-optic response and net rf power into SAW versus frequency. The clear-cut correspondence in the position of the two plots leads to the conclusion that the irregular structure in the acousto-optic response is due to rf matching irregularities.

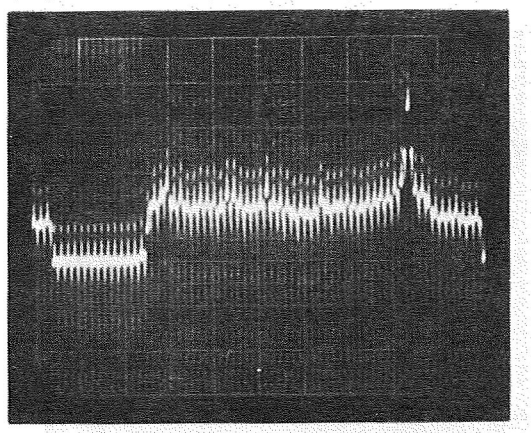

DETECTOR/CCD OUTPUT FOR A 725 MHz/100 mW
RF SIGNAL APPLIED TO THE IOSA

HORIZONTAL: 20 μs/DIV

VERTICAL: 50 mV/DIV

3 dB RESOLUTION: 8 MHz

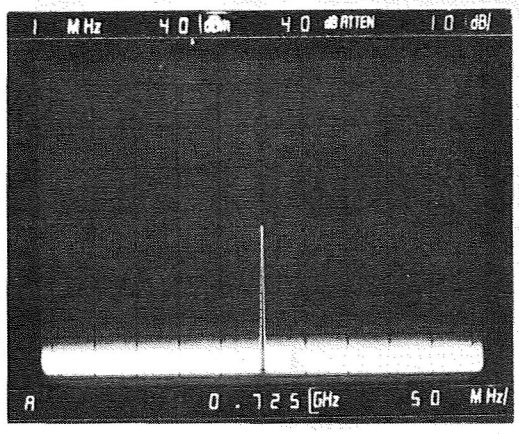

Figure 20.- Single-tone frequency resolution on the IOSA device. Sample 4.

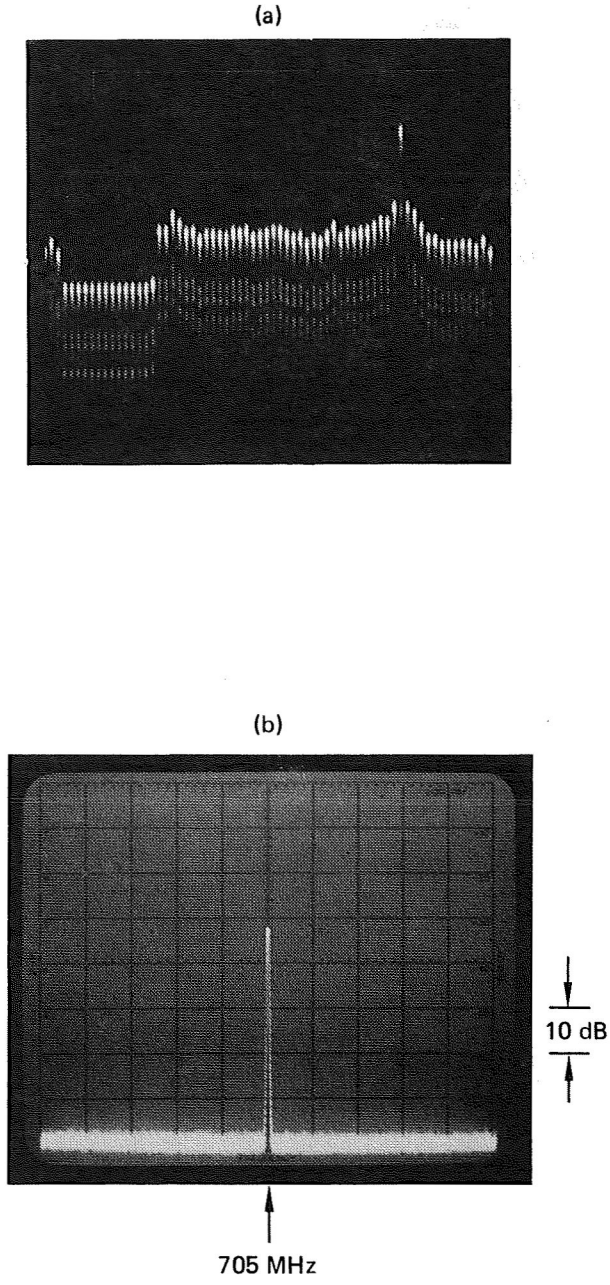

Figure 21.- Response from one half of the detector/CCD array when driven by a 100 mW, 705 MHz rf signal. (Vert: 50 mV/div, Horiz: 20 μsec/div).

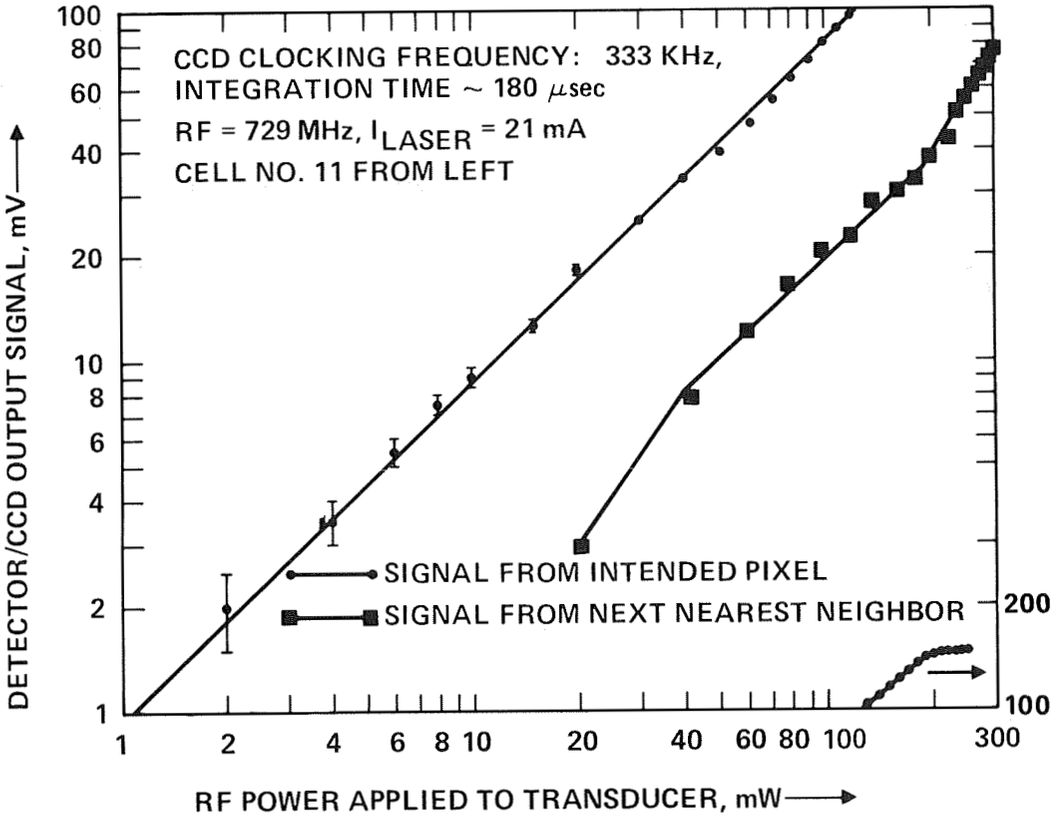

Figure 22.- Dynamic range and cross talk measured at a CCD clocking frequency of 333 kHz (Sample 4, HLP 2400 laser, pixell 11 from the left).

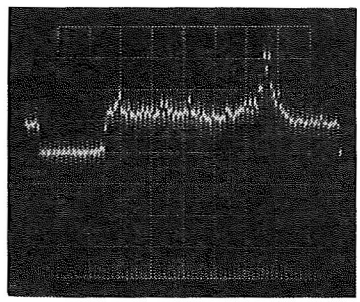

(a)

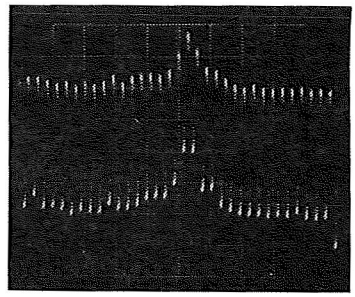

(d)

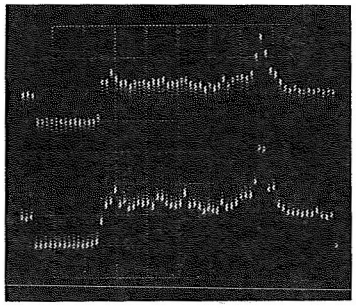

(b)

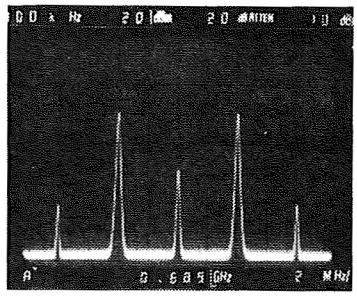

(e)

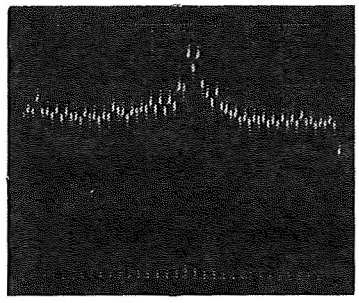

(c)

VERTICAL SCALE: 50 mV/div FOR a), b), c) AND d). a) AND c) COMPOSITE 100 ELEMENT DISPLAY. HORIZONTAL SCALE: 20 μsec/div AND 10 μsec/div. b) AND d) SEPARATE DISPLAY OF THE TWIN DETECTOR ARRAY CHANNELS. HORIZONTAL SCALE: 20 μsec/div AND 10 μsec/div

Figure 23.- Two-tone response on Sample 4, ΔF=8 MHz, F_o=689 MHz, $(P_{rf})_{tot}$=200 mW, HLP 2400 laser, I_{laser}=21 mA.

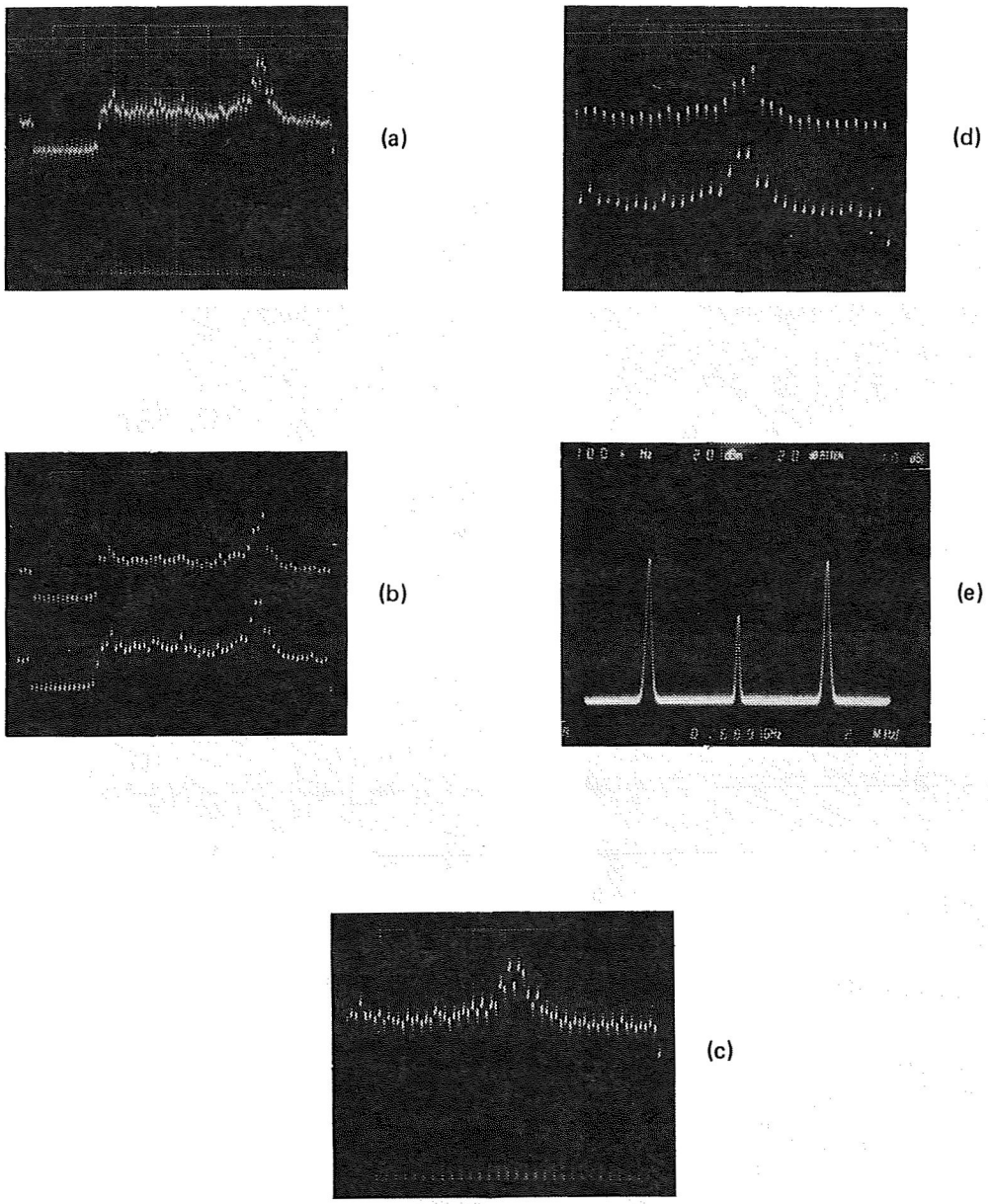

VERTICAL SCALE: 50 mV/div FOR a), b), c) AND d). a) AND c) COMPOSITE 100 ELEMENT DISPLAY. HORIZONTAL SCALE: 20 μsec/div AND 10 μsec/div. b) AND d) SEPARATE DISPLAY OF THE TWIN DETECTOR ARRAY CHANNELS. HORIZONTAL SCALE: 20 μsec/div AND 10 μsec/div

Figure 24.- Two-tone response on Sample 4, ΔF=12 MHz, F_o=689 MHz, $(P_{rf})_{tot}$=200 mW, HLP 2400 laser, I_{laser}=21 mA.

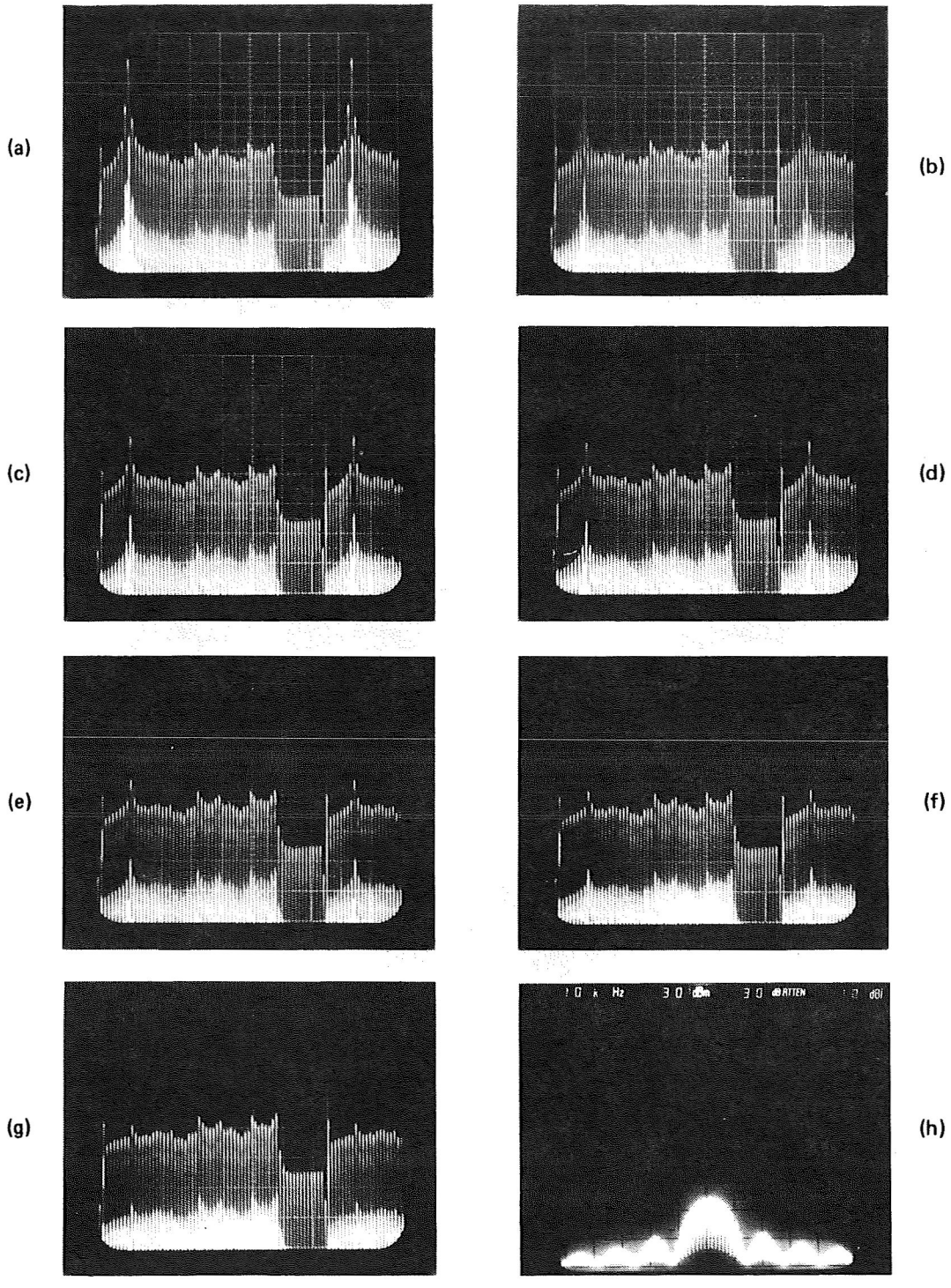

Figure 25.- RF pulse measurements. CCD clocking frequency 1.67 MHz. I_{laser}=27 mA, Vert scale: 50 mV/div, Horz. 5 µsec/div. a) cw rf power 100 mW. Pulse duty factors: b) 0.5, c) 0.4, d) 0.3, e) 0.2, f) 0.1 and g) 0. h) display the rf spectrum of a pulse train with a duty factor 0.1.